The Origin of Oxygen Vacancies Controlling $La_{2/3}Sr_{1/3}MnO_3$ Electronic and Magnetic Properties

Haizhong Guo, Jia-ou Wang, Xu He, Zhenzhong Yang, Qinghua Zhang, Kui-juan Jin, Chen Ge, Ruiqiang Zhao, Lin Gu,* Yaqing Feng, Wenjia Zhou, Xiaolong Li, Qian Wan, Meng He, Caihao Hong, Zhiying Guo, Can Wang, Huibin Lu, Kurash Ibrahim, Sheng Meng, Hao Yang, and Guozhen Yang*

Mixed-valence manganites gain increasing attentions thanks to their extraordinary properties including half-metallicity and colossal magnetoresistive response, rendering them ideal candidate for oxide spintronics applications. Oxygen vacancies in oxides have been approved to be important functional defects and are effective to manipulating their multifunctional properties. To gain a deep insight into the roles of oxygen vacancies on regulating the atomic structure and electronic properties of the mixed-valence manganites, two high-quality epitaxial $La_{2/3}Sr_{1/3}MnO_3$ films around a critical point (without/with oxygen vacancies) were designed and fabricated. From the experiments and theoretical calculations, it was found that the oxygen vacancies induce a weakening of Mn–O–Mn hybridized bond and an increase of concentration of Mn^{3+} ions, impair the double exchange between Mn^{3+} and Mn^{4+}, and therefore lead to the transition from metal to insulator and the degraded magnetic properties. Our finding demonstrates a practical approach to tune the magnetic and transport properties of oxide thin films by precisely controlling the oxygen vacancies for high performance spintronics applications.

1. Introduction

Mixed-valence manganites, $Re_{1-x}A_xMnO_3$ (where Re = rare earth, A = alkaline earth), gain increasing significance due to their fantastic rich properties as well as potential applications in oxide spintronics devices.[1–9] This variety of attractive properties arises from a delicate interaction between charge, magnetic, orbital, and structural degrees of freedom to deliver exotic magnetic and electronic phases that coexist. Desirable tunable properties, such as colossal magnetoresistance and half-metallicity of $La_{1-x}Sr_xMnO_3$, a prototype of the family of $Re_{1-x}A_xMnO_3$, are promising for multifunctional devices, such as solid oxide fuel cells, all-oxide spin FETs, magnetic tunnel junctions, and multiferroic memory.[10–12] However, oxygen vacancies will be readily induced in perovskite oxide thin films during deposition and will play a crucial role on regulating the electronic and magnetic properties of perovskite oxide thin films.[13] The effects of the oxygen vacancies on the properties of the oxide films have two aspects. On one hand, oxygen vacancies can bring out novel phenomena and various possibilities for multifunctional device applications,[14–17] in which oxygen vacancies can move through the films and modify the structural properties around them. The effects of the oxygen vacancies have not been clear yet. On the other hand, oxygen vacancies induce the degraded ferromagnetism and transport properties in mixed-valence manganite films.[18–23] Full spin polarization and half-metallicity, which are required to reach high spin injection efficiency in spintronic devices, are damaged in oxygen deficient films. In these

---

Dr. H. Z. Guo, X. He, Z. Z. Yang, Dr. Q. H. Zhang, Prof. K.-J. Jin,
Dr. C. Ge, Dr. R. Q. Zhao, Prof. L. Gu, Y. Q. Feng, Dr. W. J. Zhou,
Q. Wan, M. He, Prof. C. Wang, Prof. H. B. Lu,
Prof. S. Meng, Prof. G. Z. Yang
Beijing National Laboratory for Condensed Matter Physics
Institute of Physics
Chinese Academy of Sciences
Beijing 100190, China
E-mail: kjjin@iphy.ac.cn; l.gu@iphy.ac.cn

Dr. J.-O. Wang, Dr. C. H. Hong, Dr. Z. Y. Guo, Prof. K. Ibrahim
Beijing Synchrotron Radiation Facility
Institute of High Energy Physics
Chinese Academy of Sciences
Beijing 100049, China

Prof. K.-J. Jin, Prof. L. Gu, Prof. S. Meng, Prof. G. Z. Yang
Collaborative Innovation Center of Quantum Matter
Beijing 100871, China

Dr. X. L. Li
Shanghai Synchrotron Radiation Facility (SSRF)
Shanghai Institute of Applied Physics
Chinese Academy of Sciences
Shanghai 201204, China

Prof. H. Yang
College of Science
Nanjing University of Aeronautics and Astronautics
Nanjing 211106, China

DOI: 10.1002/admi.201500753

manganites, the transport and magnetic properties are related to the double exchange mechanism, in which e_g electrons of Mn ions hop through the bridges of oxygen atoms. The electron–lattice interaction, especially the Jahn–Teller effect is also important in the transport and magnetic mechanism. By introducing oxygen vacancies, some of the bridges for the double exchange are changed, and the local lattice distortion are introduced.[24–28] How these changes are related with the macroscopic properties still needs to the investigated. Clarifying the role of oxygen vacancies in manganite thin films is interesting not only for device applications but also for basic understanding of physical interactions in oxides.

In this work, to investigate the role of oxygen vacancies playing on regulating the electronic and magnetic properties of $La_{1-x}Sr_xMnO_3$, we grew two optimally doped $La_{2/3}Sr_{1/3}MnO_3$ (LSMO) films on the (001)-oriented $SrTiO_3$ (STO) substrates under different oxygen pressures: 10 Pa (low pressure, with some oxygen vacancies) and 40 Pa (high pressure, with proper stoichiometry), which will be referred to as LP and HP, respectively. These two oxygen partial pressures were chosen just below and above a critical oxygen pressure »26 Pa, since it was reported that oxygen vacancies would be induced in LSMO films with oxygen pressure below 26 Pa during growth.[22,29] The evolution of atomic structure and electron correlation in LSMO thin films with oxygen vacancies was investigated employing a combination of high-resolution synchrotron X-ray diffractometry (SXRD), scanning transmission electron microscopy (STEM), X-ray photoemission, X-ray absorption spectroscopy (XAS), resonant X-ray photoemission spectroscopy, and band structure calculations, etc. It was found that the distribution of the oxygen vacancies is nonuniform in LP, and oxygen vacancies induce an increased concentration of Mn^{3+} ions and the weakening of the Mn—O hybridized bond. The oxygen vacancies cause the Mn^{4+}–O–Mn^{3+} states to decline to Mn^{3+}–O–Mn^{3+} states and impair the double exchange between Mn^{3+} and Mn^{4+}, resulting in the transition from metal to insulator and the degraded transport and magnetic properties.

2. Results and Discussion

2.1. The Crystal Structure and Lattice Parameters Identified by SXRD and RMS

The crystalline quality and lattice constants of the LSMO thin films were identified by high-resolution SXRD. The SXRD θ–2θ scan curves (Figure 1S, Supporting Information) indicate that LP and HP are both epitaxially grown along the *c*-axis orientation with a good single phase, and the out-of-plane lattice constant of LP is larger than that of HP. To further gain the in-plane lattice parameters and the exact crystal structures, we also performed the high-resolution SXRD reciprocal space mapping (RSM) experiments. **Figure 1**a,b shows the high-resolution *HL* RSMs around the (002) STO reflection of LP and HP, respectively. *H*, *K*, and *L* are reciprocal space coordinates. It can be seen from Figure 1a,b that both RSM spots of LP and HP almost have the same *H* values as that of the STO substrate, indicating that both the (*00l*) planes of LSMO films are parallel to the STO substrate and both LP and HP were grown coherently on the STO substrates, as $[00l]_{LSMO}//[00l]_{STO}$. To further characterize the crystal structure of the LSMO films, *HK* RSMs around (002) LSMO diffraction were also measured. It was confirmed from *HK* RSMs around (002) LSMO diffraction peak (not shown here) that single peak structure without any other structure was observed, indicating that there is no existence of the rotated twinning structure or structural domains in LP or HP.

RSMs around (002) only show the information on the spacing of lattice planes in the out-of-plane direction, and RSM diffraction patterns around other diffractions will provide more information on the crystal structure and lattice parameters. Therefore, RSM diffraction patterns around (013) STO and (113) STO were also measured, and the high-resolution *HL* RSMs around the (013) STO reflection are shown in Figure 2Sa,b (Supporting Information). It can be seen from Figure 2Sa,b (Supporting Information) that LSMO RSM spots around (013) diffraction exhibit only single peak structure, no hints of splitting into two or more spots. According the schematics of reciprocal lattices parallel to the *H–L* plane of cubic substrate, the single diffraction spots of the *HL* RSMs ($H \neq L$) of the films around the (0*HL*) and (*HHL*) cubic substrate indicate that the film is at tetragonal or cubic phase.[30,31] The single peaks of the *HK* RSMs around (013) LSMO diffraction structures further confirm that there is no existence of other structural domains or the rotated twinning structure of the LSMO lattice in both LP and HP. *HK* RSMs around (013) LSMO diffraction are shown in Figure 2Sc,d (Supporting Information). It can be clearly seen from *HK* RSMs around (013) LSMO diffraction peak that single peak structure without any other structure was observed, further indicating that there is no existence of the rotated twinning structure or structural domains in LP or HP. The results of RSMs around the (113) diffraction peaks (not shown here) also confirm the same conclusions. From the RSM results around LSMO (002), (013), and (113) peaks, the crystal structures and lattice parameters of LP and HP were determined. The results of the RSMs indicate that LP and HP are both at tetragonal phase. It was well known that in contrast to other manganites, tilt of MnO_6 octahedra in $La_{1-x}Sr_xMnO_3$ is rather small and its lattice can be treated as tetragonal.[32] Therefore, the tetragonal structure in both LP and HP is easily understood. The out-of-plane lattice constants of LP and HP are about 3.8744 and 3.8603 Å, respectively, and the in-plane lattice constant of the films perfectly matches that of the STO substrates (a = 3.9050 Å). Since the oxygen vacancies exist in the LSMO films grown with oxygen pressure below 26 Pa,[22,29] we would ascribe this expansion of the lattice constant of LP to the effect of the oxygen vacancies. Oxygen vacancies are double donor defects, and the nearest two $Mn^{3+/4+}$ and four La^{3+}/Sr^{2+} cations of a +2 charged oxygen vacancy are displaced away from it, thus inducing the expansion of the volume of unit cell. This also indicates the modification of the Mn valence states due to the direct coupling between Mn ions and oxygen vacancies, which will be discussed later.

2.2. Influences of Oxygen Vacancies on the LSMO Microstructures Investigated by STEM

To further characterize the difference between the microstructures of LP and HP, state-of-the-art sophisticated spherical

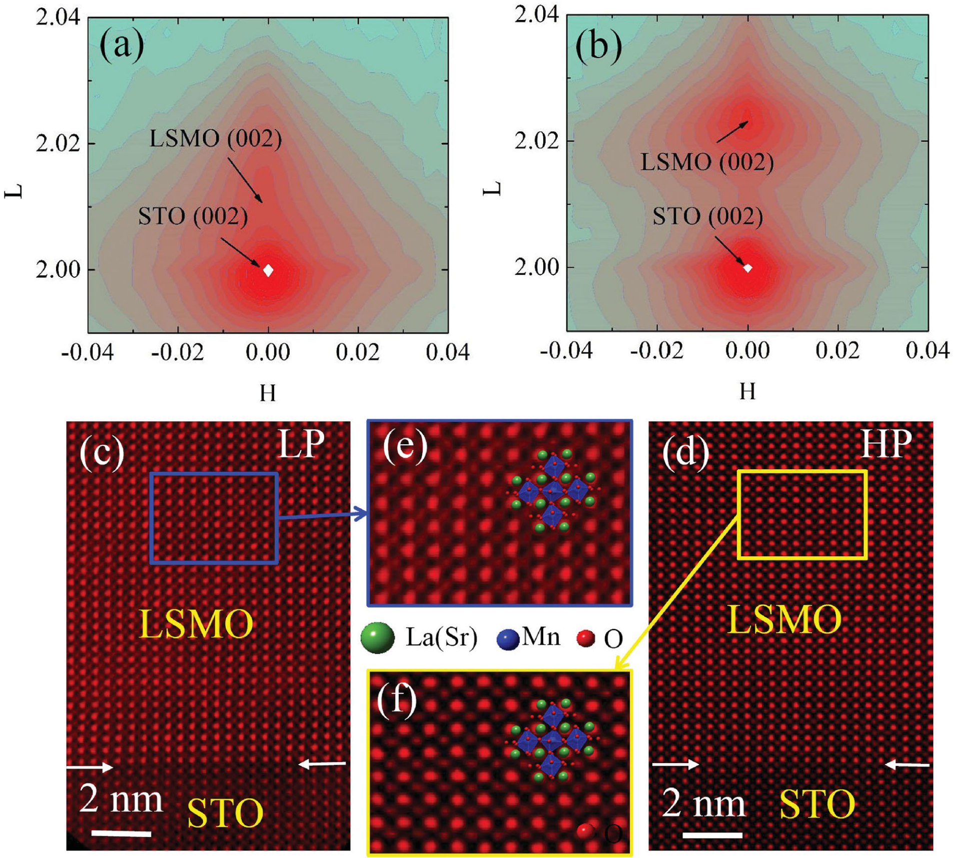

Figure 1. *HL* reciprocal space mappings around STO (002) for a) LP and b) HP, respectively. Atomically resolved HAADF images of c) LP and d) HP near the interface viewed along the [100] direction. The enlarged parts of e) LP and f) HP with the same area marked by the blue and olive boxes in panels (c) and (d), respectively. The insets of panels (e) and (f) show the corresponding structure models for LP and HP, respectively.

aberration-corrected STEM techniques combined with the high-angle annular dark-field (HAADF) and annular-bright-field (ABF) techniques were utilized. The contrast of HAADF and ABF images exhibit »$Z^{1.7}$ and $Z^{1/3}$ dependence, respectively, where Z is the atomic number,[33] therefore, different kinds of atom columns can be clearly distinguished (i.e., in HAADF images, the largest contrast indicates La(Sr) columns, weaker contrast denotes Mn, while the weakest contrast of oxygen columns only can be seen in ABF images). Figure 1c,d shows the HAADF-STEM images of LP and HP near the interface region, respectively. It can be seen that the both interfaces of LP and HP are atomically sharp and coherent, without any evidence of misfit dislocations or chemical reaction in the interface region, attributed to the good lattice match (»0.89% tensile strain). The excellent unit-cell to unit-cell epitaxial relationship of (001)$[100]_{\mathrm{LSMO}}$//(001)$[100]_{\mathrm{STO}}$ between the LSMO films and the STO substrates can also be identified in Figure 1c,d, and the atomic stacking sequence at the interface is LaO/TiO_2. The enlarged parts of LP and HP marked by the blue and yellow boxes in Figure 1c,d, shown in Figure 1e,f, respectively, clearly illustrate that the epitaxial quality of LP and HP is extremely high. The insets of Figure 1e,f show the corresponding structure models for LP and HP with all atomic positions of La (Sr), Mn, and O, respectively. The fast Fourier transforms (FFTs) of LP and HP shown in Figure S3a,b (Supporting Information), respectively, both correspond to the tetragonal structure, which is in consistent with the SXRD results. In addition, the FFT images also demonstrate that slight lattice expansion in LP samples along the out-plane direction, also in consistent with the SXRD results.

To obtain direct evidences of the existence of oxygen vacancies in LP, STEM imaging was conducted under ABF mode, which is extremely sensitive to the presence of oxygen vacancies.[16,20,33–36] **Figure 2**a,b exhibits the ABF-STEM images of LP and HP, respectively, and the comparison between LP and HP is very obvious. It can be seen from Figure 2b that it essentially appears defect-free in HP, showing uniform contrast and atom columns. Neither grain boundaries nor strain fields are found, indicating the structure quality of HP is extremely high. However, there are some regions of accumulated strain in LP (the area showing different color contrast, fenced by the blue dotted lines in Figure 2a). These regions of accumulated strain should result from the presence of oxygen vacancies. The atom columns of La, Mn, and O are well distinguished according to the image contrast, and oxygen atoms are in the MnO_2 layers, as demonstrated by the line profiles marked by the red boxes. It should be noted that the occupancy of oxygen column is proportional to the height of the “O valley” as marked by the red arrows on two line profiles. From the line profiles in Figure 2c,d, it is worth noting that the profile in HP is almost identical, and

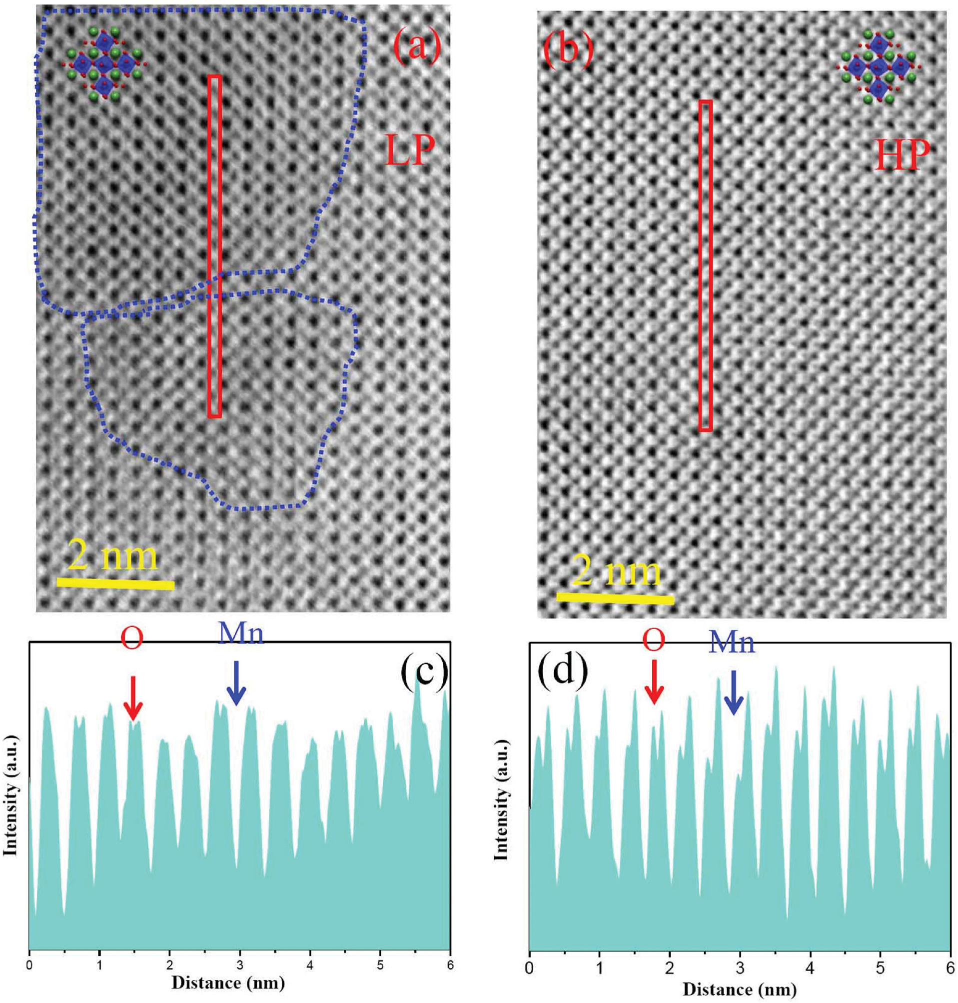

Figure 2. Atomically resolved ABF images of a) LP and b) HP along the [100] direction. Line profiles of the MnO_x layer were indicated by the red boxes for c) LP and d) HP, respectively. The insets show the corresponding structure models. The areas fenced by the blue dotted lines in panel (a) are some regions of accumulated strain, showing different color contrast. The insets of panels (a) and (b) show the corresponding structure models for LP and HP, respectively.

exhibits ordering, indicating HP has a high structural quality with proper oxygen stoichiometry. However, the height of "O valley" in the LP profile is relatively lower and fluctuant, indicating that there are many oxygen vacancies existing in LP and the distribution of the oxygen vacancies is nonuniform.

2.3. Oxygen Vacancies Regulating Electronic Structures Investigated by Synchronic XAS, XPS, XMCD, and RPES

The spectral splitting of the 3*s* core-level X-ray photoemission spectra (XPS) in transition metals and their compounds originates from the exchange coupling between the 3*s* holes and the 3*d* electrons. The relationship between magnitude of the Mn 3*s* splitting (ΔE_{3s}) and the Mn valence V_{Mn} was calculated by employing the following linear equation[37]

$$V_{Mn} = 9.67 - 1.27\Delta E_{3s} / \text{eV} \quad (1)$$

The Mn 3*s* XPS results are exhibited in **Figure 3**a, and ΔE_{3s} is about 5.085 and 4.976 eV for LP and HP, respectively, resulting in V_{Mn} about 3.212 and 3.350. The smaller formal valence of Mn ions in LP is confirmed to be induced by the oxygen vacancies in LP. A similar increase of the splitting due to the decrease of the Mn formal valency induced by oxygen vacancies was also observed in $La_{0.7}Ca_{0.3}MnO_3$ thin films.[38] However, Picozzi et al.[19] reported an opposite trend between the Mn 3*s* splitting and the oxygen vacancies in LSMO thin films, and they explained this controversy considering the effects of the increase of the Mn bonding covalency in the LSMO thin films with oxygen vacancies. The results of Picozzi et al. were obtained with the assumption of no structural relaxation. Therefore, the Mn hybridization is overestimated. To further examine the effect of the oxygen vacancies on the electronic structures, we examined the XAS with total electron yield (TEY) mode at the Mn $L_{2,3}$ and O *K* edges in LP and HP. The Mn-$L_{2,3}$ XAS spectra correspond to on-site transitions of the form $2p^6 3d^n \rightarrow 2p^5 3d^{n+1}$ and present two groups of multiplets, namely

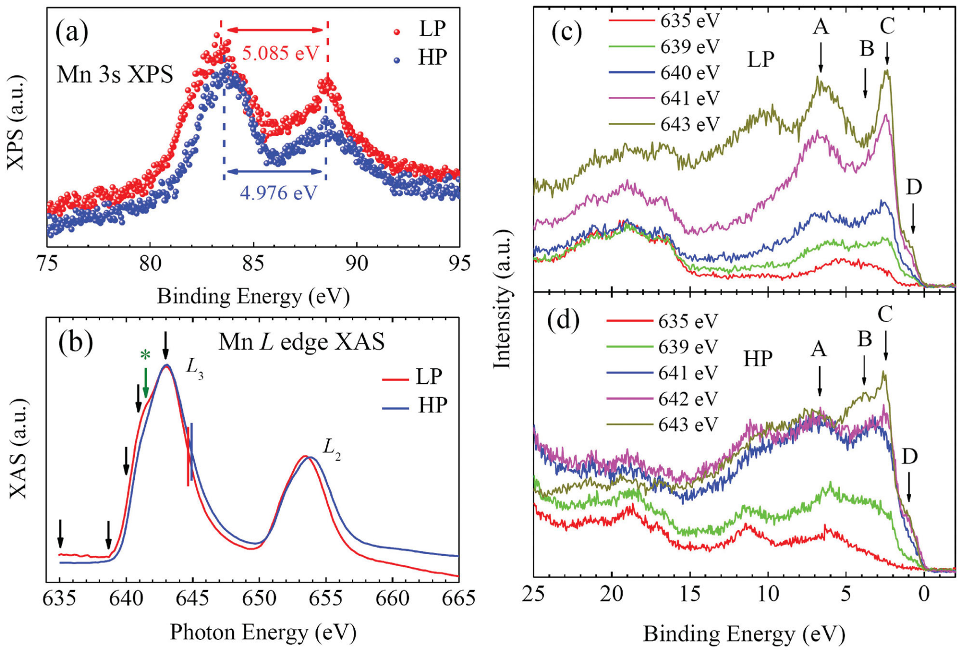

Figure 3. a) The Mn 3*s* XPS spectra for LP and HP, respectively. The energy separation between two Mn 3*s* peaks indicates ΔE_{3s}. b) The XAS spectra at the Mn $L_{2,3}$ edge for LP and HP, respectively. The excitation energies used in the RPES measurements are indicated by black arrows. Mn 2*p*-3*d* RPES spectra of c) LP and d) HP, respectively. The olive star indicates an obvious enhancement of the shoulder of the spectrum feature of LP.

the L_3 ($h\upsilon$ » 639–648 eV) and L_2 ($h\upsilon$ » 650–656 eV) white lines regions, split by the spin-orbit interaction of the Mn 2*p* core level. The line shape of the spectrum depends strongly on the multiplet structure given by the Mn 3*d*-3*d* and 2*p*-3*d* Coulomb and exchange interactions, as well as by the local crystal fields and the hybridization with the O 2*p* ligands. It can be seen from Figure 3b that there are some slight changes in the spectra between these two samples. First, the Mn *L* spectra shift to lower photon energy in LP than that in HP. This chemical shift is caused by changes in the electrostatic energy at the Mn site driven by the decrease in the 3*d* count,[39] indicating the Mn oxidation state is reduced via the creation of oxygen vacancies in LP. Second, the spectrum changes shape a little and there is an obvious enhancement of the shoulder of the spectrum feature at the low photon energy side of the L_3 peak (indicated by the olive star) in LP, which is originating primarily from Mn^{3+} valence state.[39,40] The change of shape is expected due to the sensitivity of the transition-metal spectra to the symmetry of the ground state. These signatures imply that there is an increased concentration of Mn^{3+} ions in LP due to the existence of the oxygen vacancies, which are confirmed by the ABF STEM results.

XAS at the O *K*-edge (1*s*→2*p* dipole transitions) is an important tool to study the electronic structure in perovskite oxide thin films.[39,41] In manganites the pre-edge feature around 528.5eV reflects the O 2*p* hole induced by the strong hybridization with the Mn 3*d* $e_g\uparrow$ and $t_{2g}\downarrow$ unoccupied states of the Mn^{4+} sites.[42,43] The spectrum of HP (Figure 5S, Supporting Information) displays a double-peak splitting feature compared with a single broad peak in LP. The double-peak splitting feature in HP corresponds to the O 2*p* holes resulting from hybridization with the Mn^{4+} 3*d* $e_g\uparrow$ and $t_{2g}\downarrow$ unoccupied states at the low and high energies, respectively, similar to that of the $La_xSr_{1-x}MnO_3$.[37] Usually, in bulk, the energy splitting does not appear with the existence of the oxygen vacancies since the local tetragonal Jahn–Teller distortion is expected to affect only the Mn^{3+} sites, not the Mn^{4+} sites.[43,44] The Jahn–Teller distortion removes the degeneracy of the $e_g\uparrow$ and $t_{2g}\downarrow$ levels leading to an experimentally nonresolved energy difference between them, i.e., a broad single peak spectral structure.[44] Another reason for the smearing out of the double peak is more likely to be the result of the mixing of the oxygen octahedron and tetrahedron symmetry. In oxygen tetrahedron, where an oxygen vacancy is present, the degeneracy of e_g and t_{2g} levels are removed. From a double-peak splitting feature to a single broad peak with oxygen vacancies in the O XAS pre-peak, it is clearly shown that the electronic structure of perovskite oxide thin films would be modified by the oxygen vacancies.

In order to study the influence of oxygen vacancies on the valence-band electronic structure of LSMO, we performed Mn 2*p* resonant photoemission spectroscopy (RPES) measurements, by which the density of states (DOS) associated with the Mn 3*d* electron is so enhanced that the valence-band states near Fermi edge are expected to be clearly observed.[40] Figure 3c,d exhibits the resonantly enhanced valence-band spectra of the LSMO thin films. In the photon energy range spanned by the resonance indicating by the arrows in Figure 3b (635 eV for the nonresonance and 643eV for the resonance), strong enhancement of the Mn 3*d* spectral intensity is observed. In comparison with the cluster model calculation, the enhanced states C and D in Figure 3a,b (about 2.3 and 0.6 eV) originate from the Mn 3*d* $t_{2g}\uparrow$ and $e_g\uparrow$ states, respectively, while the other states at higher energy (as labeled A and B) are assigned as Mn 3*d* strongly hybridized with the ligand O 2*p* states.[46,47]

Very obvious variations between the RPES spectra of LP and HP are observed, especially in the B peak. Dramatic decrease of B peak in LP during the resonant process indicates that the Mn–O hybridized bond is severely weakened. We suggest that the existence of the oxygen vacancies in LP is the reason for this phenomenon, and the weakening of the Mn–O hybridized bond cause the Mn^{4+}–O–Mn^{3+} states to decline to Mn^{3+}–O–Mn^{3+} states. The transformation of the Mn valence states and Mn–O–Mn interactions induced by the oxygen vacancies in LP would result in the degraded magnetic properties of LP, which are confirmed by the results of the X-ray magnetic circular dichroism (XMCD) spectra (Figure 6S, Supporting Information) and the magnetic property measurements (will be discussed later).

2.4. Evolution of the Oxygen Vacancies on the Electronic Structures from the Density Functional Calculations

Density functional theory (DFT) has been used to shed insight into the electronic structures with/without oxygen vacancies. **Figure 4** aexhibits the atomic structure with the oxygen vacancy sites in the LaO layers (case C in Figure 4S, Supporting Information) corresponding to $La_{2/3}Sr_{1/3}MnO_{3-1/12}$. Figure 4bexhibits the calculated DOS projected onto the Mn e_g orbitals in the case of oxygen vacancy in the C system (in the LaO layer) compared with the bulk. The calculated Mn 3*d* energy of LSMO with the oxygen vacancies shifts to lower value relative to the Fermi energy, consistent with the observed Mn *L* spectra shift to lower photon energy in LP from the XAS results. Picozzi et al.[19] found that the half-metallic behavior is destroyed by the oxygen vacancies. The band gap in the minor spin channel is destroyed by a wide defective band. However, by relaxing the structure, we found that the distance of Mn ions bonded to the oxygen vacancy becomes larger, which reducing the width of the defective band and shifting it above the Fermi level. Therefore, the spin of the Mn 3*d* electrons is fully polarized, and there is no evidence of large change of exchange splitting, suggesting that the reason for the reduction of the total magnetic moment of LP is not due to the changing of the exchange splitting, but the destroying of the long range ferromagnetic order.

We have applied Bader analysis to investigate the changes of the charge and the spin polarization of the Mn ions. The results are shown in **Table 1**, supposing that the oxygen vacancy is in the LaO plane (case C). The calculated results with oxygen vacancies in other cases show similar physics and are not shown here. The most noticeable difference is that the valence of the Mn ions directly connecting to the oxygen vacancy decreases, which accompanies the increasing of the magnetic moment. It should be noticed that the valences from

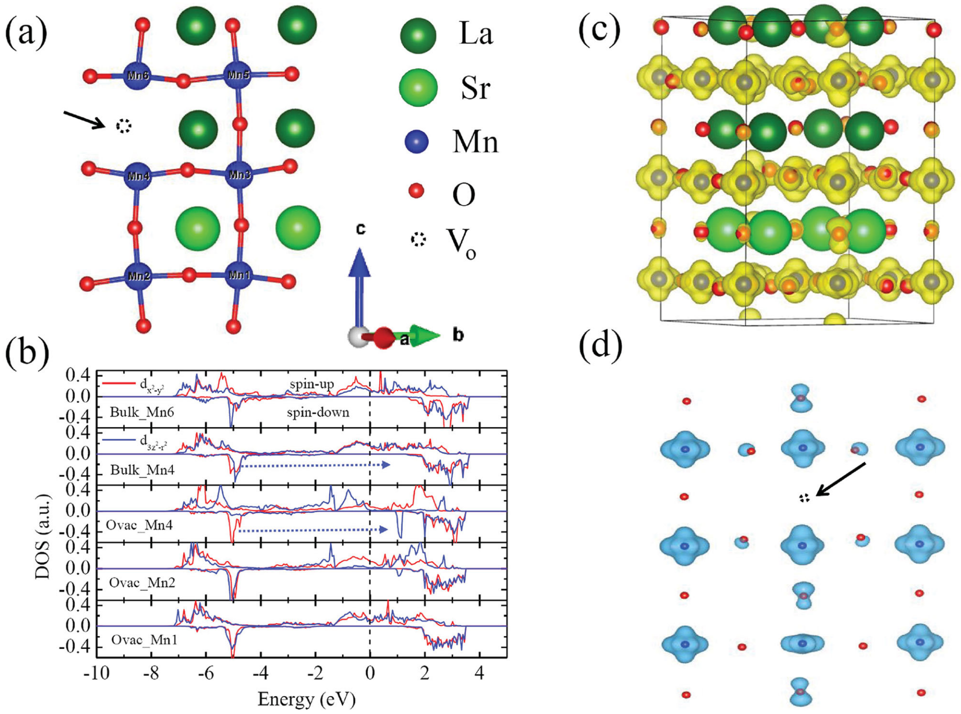

Figure 4. a) Plane-view of the schematic of the $La_{2/3}Sr_{1/3}MnO_{3-1/12}$ structure with oxygen vacancies in the LaO layers (case C in Figure 3S). b) Projected density of states (DOS) on the Mn e_g orbitals in the bulk LSMO and the $La_{2/3}Sr_{1/3}MnO_{3-1/12}$ structure with oxygen vacancies in the LaO layers. Here, red lines is for $d_{x^2-y^2}$ and blue lines for $d_{3z^2-r^2}$. The black vertical dash line is the maximum energy of occupied states. Mn1, Mn2, ...Mn6 are illustrated in panel (a). The blue dashed arrow show the shift of the $d_{3z^2-r^2}$ energy. c) Isosurface of the charge density in the energy range between −2 and 0 eV in the $La_{2/3}Sr_{1/3}MnO_{3-1/12}$ structure with oxygen vacancies in the LaO layers. d) Plane view of the charge density in the energy range between −2 and 0 eV in the $La_{2/3}Sr_{1/3}MnO_{3-1/12}$ structure with oxygen vacancies in the LaO layers. Olive spheres represent La atoms, green spheres represent Sr atoms, blue spheres represent Mn atoms, and red spheres represent oxygen atoms, respectively. Oxygen vacancy is highlighted by the black dashed circles and arrows. In structure without oxygen vacancies, there are two in equivalent Mn sites, which are surrounded by La only (Mn6) and surrounded by both La and Sr (Mn2).

Table 1. Bader charge of the atoms in the structure.

	Without vacancy		With vacancy	
	Valence	Spin	Valence	Spin
Mn1	1.95	3.92	1.95	3.95
Mn2	1.95	3.92	1.99	3.84
Mn3	1.95	3.92	1.91	4.14
Mn4	1.95	3.92	1.80	4.23
Mn5	1.96	3.91	1.88	4.19
Mn6	1.96	3.91	1.77	4.29

Bader analysis are usually smaller than what the valences is conventionally defined. The results are consistent with the XAS data. The oxygen vacancy can be seen as electron donors, and decrease the number of the holes in LSMO, and can impair the double exchange between Mn^{3+} and Mn^{4+}.

The Jahn–Teller type distortion caused by the tensile strain shifts the energy of the in-plane orbitals down and rises those of the out of plane orbitals in the LSMO. Here we assume that the Mn—O—Mn chain where the O is missing is along the z direction. The octahedral symmetry is broken and the O ions form a tetrahedron. Because that the Coulomb repulsive interaction between the O 2*p* electrons and the Mn 3*d* electrons, especially for those at the $d_{3z^2-r^2}$ orbitals which are along the Mn—O bonds, the energy of the $d_{3z^2-r^2}$ of the Mn ions bonding to the oxygen vacancies are shifted down, and are thus preferably occupied, as shown in Figure 4c,d. The removing of the oxygen causes the breaking of the attraction force between the Mn and O ions, therefore the repulsion force of the two Mn ions push them far away from each other, which is the driving force of the expansion of the lattice. The calculated volume of the LSMO bulk is 58.6 Å^3 per unit cell, while that with oxygen vacancy is 58.8 Å^3, about 0.2% larger. The values from XRD results give a 0.3% expansion in volume, indicating that the concentration of the oxygen vacancies is larger than 1/12 vacancies per unit cell (i.e., 0.28% O ions). This also results in the squeezing of the Mn—O octahedron along the *z*-direction which shares the vertex of oxygen with the tetrahedrons in the *z*-direction. The result is that the energy of the $d_{3z^2-y^2}$ orbital of the Mn in the cage of that octahedron is shifted down, and that orbital is preferably occupied, as in Figure 4d.

From Figure 4, we can also see that the reduction of the density of states projected on the $d_{3z^2-r^2}$ orbital at about –5 eV, which can be interpreted as the bonding state of the hybridized O 2*p*-Mn $d_{3z^2-r^2}$ state. With removing the O atom, this hybridization is also removed. The electrons thus occupy the states at higher energies (mostly nonhybridized 3*d* states of Mn). This effect is especially clear in the down spin channel as shown in Figure 4b. Because the Mn e_g energy is much higher than the O 2*p* state, the occupied Mn e_g electrons are almost all from the Mn e_g–O *p* hybridization. Once the hybridization is broken, the density of these states is all removed. This corresponds to the lower peak B in LP than in HP in RPES results (as shown in Figure 3) which showing the weakening of the Mn—O hybridization.

In LSMO, the rotation and tilting of the oxygen octahedral are small and consequently the Mn—O—Mn bond angles are large. The oxygen vacancies can lead to smaller bond angles. The double exchange of the conducting electrons on the Mn sites is through the bridge of the oxygen in between, therefore, is largely affected by the bond angles. The decreasing of the bond angles can be another reason for the weakening of the Mn—O hybridization and the ferromagnetic double exchange interaction between Mn sites.

Our calculation results do not show a reduction in total magnetic moment or the insulating state. The main difference is that the calculation failed to give the same magnetic structure in the structure with oxygen vacancies. Instead, a ferromagnetic ground state is given. To predict the right magnetic ground state with DFT+*U* in the manganite is quite subtle. By carefully tuning the effective *U* and *J*, some magnetic structure fit the experiments can be given, but it does not always give the right result in all cases with the same *U* and *J*. There are also something missing from the DFT calculations like the phase separation, and the Anderson localization effect, which could be responsible for the suppressed magnetic moments and insulating state. Despite that, comparing the calculation and experimental result can give us some hint on what the roles the oxygen vacancies play in the LSMO.

2.5. Influences of the Oxygen Vacancies on the Physical Properties

Figure 5 exhibits the magnetization and resistivity of LP and HP as a function of temperature, and a large variation of magnetic and transport characteristics are observed. It can be seen from Figure 5b that HP displays a typical $M(T)$ curve for LSMO and a sharp paramagnetic-to-ferromagnetic phase transition occurs at the Curie temperature T_C » 350 K. Here, T_C is defined as the temperature where (dM/dT) reaches the extreme value. T_C is slightly lower than that of bulk (T_C » 360 K),[29,48] but as high as the ever reported value of the thin films with proper oxygen stoichiometry.[49] Whereas, $M(T)$ of LP differs from standard ferromagnetic behavior with the degraded magnetic properties, exhibiting a broad paramagnetic-to-ferromagnetic crossover at T_C » 169 K with a low magnetization value. Even so, both LP and HP are obviously ferromagnetic below T_C, exhibiting ferromagnetic hysteresis loops at low temperature. The hysteresis loops at 10 K were shown in the inset of Figure 5a,b measured after field cooling in 200 Oe. The hysteresis loop of HP has the characteristics of a soft magnet with a low coercive field (H_C = 95 Oe) and a saturation magnetization (M_S) of 3.54 μ_B/Mn at 10 K, which approaches the bulk value (11/3 μ_B/Mn).[48] Compared to HP, the hysteresis loop of LP is degraded and sheared with a larger coercive field. And the saturation magnetization of LP is very low (M_S » 0.66 μ_B/Mn at 10 K). The magnetic characteristics of the sharp magnetic phase transition, low coercive field, high saturation magnetization, and high Curie temperature in HP indicate that HP exhibits high-quality magnetic properties with the proper oxygen stoichiometry, the magnetic properties consistent with previous reports of the LSMO films and bulks with the proper oxygen stoichiometry.[48–50] One also can notice in Figure 5c,d that HP is metallic while LP is insulating. A typical metal-to-insulator transition (T_P) accompanied by the paramagnetic-to-ferromagnetic

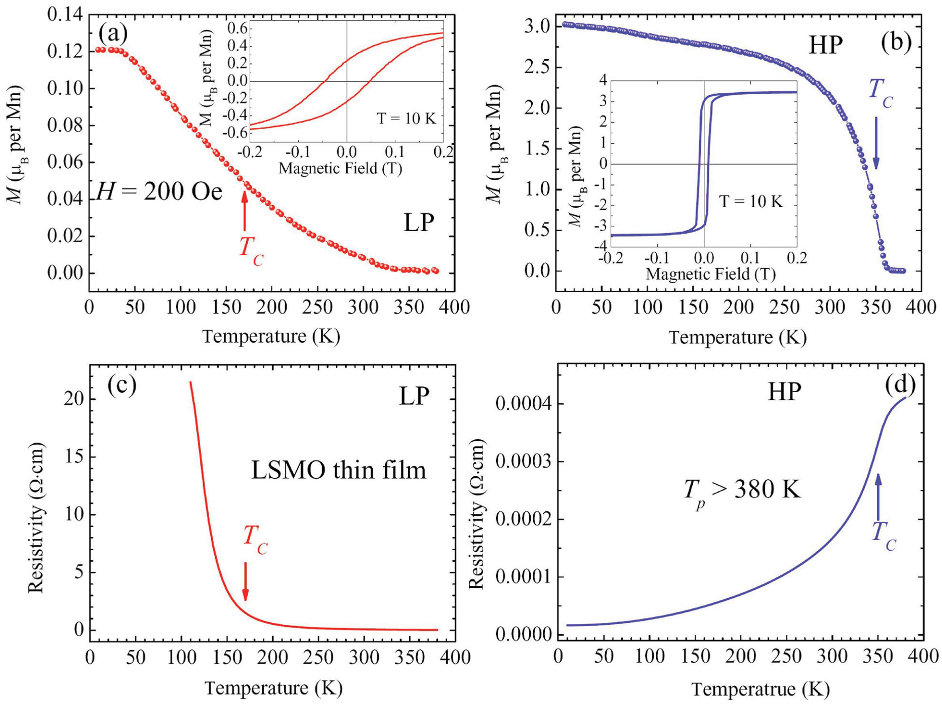

Figure 5. (SQUID) Magnetization versus temperature with an applied magnetic field of 200 Oe (field cooling) for a) LP and b) HP, respectively. Resistivity versus temperature for c) LP and d) HP, respectively. Insets of panels (a) and (b): hysteresis loops of LP and HP measured at 10 K, respectively.

occurring at T_C in either LSMO bulks or thin films with proper oxygen stoichiometry, however, is not be seen in our measured regime due to our measurement limit. It was reported by Bertacco et al.[50] that the highest T_P is larger than 440 K in their LSMO film with T_C = 350 K. Our HP also displays a metallic behavior well above T_C, consistent with their report.[50] The degraded transport properties of LP can also be attributed to the effects of the oxygen vacancies. The oxygen vacancies will be formatted when the LSMO thin films grown below 26 Pa, inducing a charge transition disproportionation of the $Mn^{4+} \rightarrow Mn^{3+}$. The enhanced Mn^{3+} concentration may segregate into inhomogeneous patches, resulting in patches where the magnetic ordering varies from antiferromagnetic (Mn^{3+}–O–Mn^{3+}) to ferromagnetic (Mn^{3+}–O–Mn^{4+}) interactions. On the other hand, depletion of oxygen from the Mn—O—Mn chain reduces the coordination of Mn cations, destroying the Mn^{3+}–O–Mn^{4+} interactions. These would cause the degraded magnetic and transport properties in LP.

2.6. Discussion on the Role of the Oxygen Vacancy

Here we discuss the effect of the oxygen vacancy on the macroscopic properties. First, oxygen vacancies play as donors, which increase the ratio of Mn^{3+}, as is shown in the XPS results, the XAS results, and the DFT results. Therefore, the local Jahn–Teller effect is enhanced. The strong interaction between the electron and the Jahn–Teller lattice distortion, i.e., the Jahn–Teller polaron, is generally regarded as one main reason for the insulating state of LSMO at high temperature. The double exchange can melt down the Jahn–Teller polaron by the double exchange between Mn^{3+} and Mn^{4+} if the spin is parallelly aligned at low temperature as in HP. Whereas in LP, the ratio Mn^{3+}–O–Mn^{3+} configuration is higher, therefore double exchange is suppressed and LP tend to be insulating.

Second, the oxygen vacancies break the octahedron symmetry, therefore the energy of thee_g orbital pointing at the oxygen vacancy is reduced, which introduces a strong electron–lattice interaction. Like the Jahn–Teller effect, the strong electron–lattice interaction tends to localize the electrons so that the superexchange tends to dominate the magnetic interaction. According to the Goodenough-Kanamori rules,[51,52] whether the superexchange between Mn ions is ferromagnetic or antiferromagnetic is decided by the orientation of the orbital. Due to the random position of the oxygen vacancies, it is difficult to analyze the interaction between the effect of the oxygen vacancies and that of the JT distortion. However, it is clear that the suppressing of the double exchange would reduce the ferromagnetic interaction, which could be responsible for the large reduction in the total magnetic moment of LP. The difference between the oxygen vacancies and Jahn–Teller effect is that even the double exchange may not be able to compensate the strong localization tendency. Our calculation of the Bader charge shows even in the ferromagnetic state, the electrons tend to reside on the Mn site near the oxygen vacancies, while the charge distribute homogeneously without oxygen vacancies. Therefore, the electron–lattice interaction is even stronger with the oxygen vacancies.

Third, the oxygen vacancies play as local chemical pressure, which leads to the local distortion and rotation of the oxygen octahedrons (or tetrahedrons). The effect is similar to substitute A-site ions with smaller sized ions, which tends to reduce Mn—O—Mn bond angle and enhances the local Jahn–Teller effect. In manganite, the rotation of oxygen octahedron decreases the Mn—O—Mn bond angle and consequently the probability of hopping between Mn ions. The breaking of the Mn—O—Mn chain also decreases the hopping. The decrease of the Mn—O hybridization, which is proportional to the hopping integral, is shown in the RPES results and the DFT results.

Finally, the oxygen vacancies also introduces disorder. The TEM results show inhomogeneous strain in LP, which is a sign of it. The random position of the ions leads to random exchange and hopping between Mn sites. According to Moreo et al.,[53] this will result in continuous magnetic transition instead of an abrupt phase transition, and the co-existence of ferromagnetic and antiferromagnetic clusters, therefore the phase separation effect are more likely to take place.

3. Conclusion

In summary, the role of the oxygen vacancies playing on manipulating the atomic structure, electronic structure, magnetic, and transport properties of $La_{2/3}Sr_{1/3}MnO_3$, a prototype of the mixed-valence manganites, has been investigated employing a combination of the experimental measurements and band structure calculations. The SXRD and STEM results indicate that LP and HP have the almost identical excellent crystal structure, however, HP has a high structural quality with proper oxygen stoichiometry while the oxygen vacancies exist in LP. The distribution of the oxygen vacancies is nonuniform and the concentration of the oxygen vacancies is estimated to be more than 2.78%. Mn and O XAS spectra imply that the oxygen vacancies cause an increased concentration of Mn^{3+} ions in LP, consistent with the results of band structure calculations. Mn RPES results suggest that the weakening of the Mn—O hybridized bond due to the existence of the oxygen vacancies in LP cause the Mn^{4+}–O–Mn^{3+} states decline to Mn^{3+}–O–Mn^{3+} states and impair the double exchange between Mn^{3+} and Mn^{4+}, the transition from metal to insulator, and the degraded magnetic properties. Our theoretical calculations show that the valence of Mn decreases with removing the oxygen atoms. The spin of the Mn 3*d* electron is fully polarized, showing that the reduction in magnetic moment is not because of the change in the single site spin polarization, but the change of the intersite exchange interaction. Finally, the influence of the oxygen vacancies on the macroscopic properties is that the oxygen vacancies induce transition from metal to insulator and the degraded magnetic properties of LSMO films. Our findings highlight the key role of the oxygen vacancies on the structural, magnetic, and electrical properties, and demonstrate an approach to tune these properties by controlling the oxygen vacancies in oxide thin films for high performance and inspiring their potential applications.

4. Experimental Section

Sample Epitaxial Growths: Epitaxial LSMO thin films were grown epitaxially on (001) STO and Nb-doped STO (0.7 wt%) single crystals by a laser molecular-beam epitaxy system (Laser-MBE, Pascal) using an excimer XeCl laser (1.5 J cm^{-2}, 308 nm, 2 Hz) combined with a high-pressure reflected high-energy electron diffraction (RHEED) and a laser diode substrate heating unit at 800 °C. LP and HP both with the thickness of 90 nm are grown under two different oxygen pressures: 10 and 40 Pa, respectively. The 2D layer-by-layer growth mode was monitored by intensity oscillation of RHEED during growth. *SXRD and RSM Measurements*: High-resolution SXRD and RSM were performed to investigate the crystal structures of the LSMO thin films at the BL14B1 beam line of Shanghai Synchrotron Radiation Facility (SSRF), using a 1.24 Å X-rays with a Huber 5021 six-axis diffractometry. The RSM presented is plotted in reciprocal lattice units (r.l.u.) of the STO substrate (1 r.l.u. = $2\pi/3.905$ Å^{-1}).

STEM Imaging with HAADF and ABF Techniques: To characterize the crystalline structures of the LSMO thin films, state-of-the-art sophisticated spherical aberration-corrected STEM techniques combined with the high-angle annular dark-field (HAADF) and annular-bright-field (ABF) techniques were utilized. The HAADF and ABF imaging was executed using an ARM-200F (JEOL, Tokyo, Japan) STEM operated at 200 kV with CEOS Cs corrector (CEOS GmbH, Heidelberg, Germany) to cope with the spherical aberration of the probe-forming condenser lens.

XPS, XAS, XMCD, and RPES Measurements: To examine the effect of the oxygen vacancies on the core-level and valence band electronic structures, XAS, XPS, X-ray XMCD, and Mn 2*p* RPES were performed on the beamlines of the Beijing Synchrotron Radiation Facility (BSRF) at the Institute of High Energy Physics, Chinese Academy of Sciences, and the background vacuum level was 6×10^{-7} Torr.

DFT Calculations: The generalized gradient approximation (GGA) optimized for solids PBEsol exchange-correlation function[54] with density functional theory was used as implemented in the Vienna ab initio simulation package.[55] The projected augment wave[56] method and a plane wave basis set with energy cutoff of 500 eV were used. A Hubbard-*U* scheme[57] with $U = 3.0$ eV and $J = 0.5$ eV was used to better describe the on-site Coulomb interaction of the Mn 3*d* electrons. A Γ-centered $5 \times 5 \times 5$ k-point grid was used to represent the Brillouin zone. A $2 \times 2 \times 3$ pseudocubic supercell was used to represent the LSMO structure, which can be viewed as an $(LaMnO_3)_2/SrMnO_3$ superlattice along the [001] direction. The structures were relaxed with the in-plane lattice fixed to 3.905 Å, according to the SXRD and RSM results. The oxygen vacancy was introduced by taking away one oxygen atom, which corresponded to $La_{2/3}Sr_{1/3}MnO_{3}\text{-}\delta$ with δ equals to 1/12. There were four equivalent oxygen sites, which are shown in Figure 4S (Supporting Information) as A (in the $(MnO_2)_1$ layer), B (in the $(MnO_2)_2$ layer), C (in the LaO layer), and D (in the SrO layer), respectively. The calculated *c*-axis lattice parameters were 3.84 and 3.85 Å without and with oxygen vacancy, respectively.

Magnetic and Transport Properties: Temperature dependences of magnetization and resistivity of LP and HP were performed using a Physical Properties Measurement System (PPMS, Quantum Design Inc.). The standard four-point probe method was used to measure the film resistivity versus temperature ($\rho(T)$). The temperature dependences of macroscopic magnetization $M(T)$ were performed with an applied magnetic field of 200 Oe (field cooling), and hysteresis loops were measured at different temperatures.

Supporting Information

Supporting Information is available from the Wiley Online Library or from the author.

Acknowledgements

This work was supported by the National Key Basic Research Program of China (Grant Nos. 2012CB921403 and 2013CB328706), the National Natural Science Foundation of China (Grant Nos. 11574365, 10904030, 11404380, 11205235, 11134012, 11474349, 11274237, and 11004238), and the Strategic Priority Research Program (B) of the Chinese Academy of Sciences (Grant No. XDB07030200). The authors would like to thank BL14B1 beamline of Shanghai Synchrotron Radiation Facility and the beamlines of the Beijing Synchrotron Radiation Facility for technique supports.

Received: November 20, 2015
Published online: January 8, 2016

---

[1] A. Urushibara, Y. Moritomo, T. Arima, A. Asamitsu, G. Kido, Y. Tokura, *Phys. Rev. B* **1995**, *51*, 14103.
[2] M. Viret, L. Ranno, J. M. D. Coey, *Phys. Rev. B* **1997**, *55*, 8067.
[3] P. Xiang, S. Asanuma, H. Yamada, I. H. Inoue, H. Sato, H. Akoh, A. Sawa, K. Ueno, H. Yuan, H. Shimotani, M. Kawasaki, Y. Iwasa, *Adv. Mater.* **2011**, *23*, 5822.
[4] P. Mandal, S. Das, *Phys. Rev. B* **1997**, *56*, 15073.
[5] A. Asamitsu, Y. Tomioka, H. Kawahara, Y. Tokura, *Nature* **1997**, *388*, 50.
[6] A. J. Millis, *Nature* **1998**, *392*, 147.
[7] L. Zhang, C. Isael, A. Biswas, R. L. Greene, A. de Lozanne, *Science* **2002**, *298*, 805.
[8] B. B. van Aken, T. T. M. Palstra, A. Filippetti, N. A. Spaldin, *Nat. Mater.* **2004**, *3*, 164.
[9] K. Miyano, T. Tanaka, Y. Tomioka, Y. Tokura, *Phys. Rev. Lett.* **1997**, *78*, 4257.
[10] J.-H. Park, E. Vescovo, H.-J. Kim, C. Kwon, R. Ramesh, T. Venkatesan, *Nature* **1998**, *392*, 794.
[11] C. Israel, M. J. Calderón, N. Mathur, *Mater. Today* **2007**, *10*, 24.
[12] A.-M. Haghiri-Gosnet, J.-P. Renard, *J. Phys. D: Appl. Phys.* **2003**, *36*, R127.
[13] J. N. Eckstein, *Nat. Mater.* **2007**, *6*, 473.
[14] D. A. Muller, N. Nakagawa, A. Ohtomo, J. L. Grazul, H. Hwang, *Nature* **2004**, *430*, 657.
[15] A. Brinkman, M. Huijben, M. Van Zalk, J. Huijben, U. Zeitler, J. C. Mann, W. G. Van Der Wiel, G. Rijnders, D. H. A. Blank, H. Hilgenkamp, *Nat. Mater.* **2007**, *6*, 493.
[16] Z. T. Xu, K. J. Jin, L. Gu, Y. L. Jin, C. Ge, C. Wang, H. Z. Guo, H. B. Lu, R. Q. Zhao, G. Z. Yang, *Small* **2012**, *8*, 1279.
[17] P. Gao, Z. Kang, W. Fu, W. Wang, X. Bai, E. Wang, *J. Am. Chem. Soc.* **2010**, *132*, 4197.
[18] M. Rajeswari, R. Shreekala, A. Goyal, S. E. Lofland, S. M. Bhagat, K. Ghosh, R. P. Sharma, R. L. Greene, R. Ramesh, T. Venkatesan, T. Boettcher, *Appl. Phys. Lett.* **1998**, *73*, 2672.
[19] S. Picozzi, C. Ma, Z. Yang, R. Bertacco, M. Cantoni, D. Petti, S. Brivio, F. Ciccacci, *Phys. Rev. B* **2007**, *75*, 094418.
[20] H. Z. Guo, J. Burgess, E. Ada, S. Street, A. Gupta, M. N. Iliev, A. J. Kellock, C. Magen, M. Varela, S. J. Pennycook, *Phys. Rev. B* **2007**, *77*, 174423.
[21] R. Q. Zhao, K. J. Jin, Z. T. Xu, H. Z. Guo, L. Wang, C. Ge, H. B. Lu, G. Z. Yang, *App. Phys. Lett.* **2013**, *102*, 122402.
[22] A. I. Lobad, R. D. Averitt, C. H. Kwon, A. J. Taylor, *Appl. Phys. Lett.* **2000**, *77*, 4025.
[23] C. Ge, K. J. Jin, L. Gu, L. C. Peng, Y. S. Hu, H. Z. Guo, H. F. Shi, J. K. Li, J. O. Wang, X. X. Guo, C. Wang, M. He, H. B. Lu, G. Z. Yang, *Adv. Mater. Interfaces* **2015**, *2*, 1500407.
[24] C. Aruta, G. Balestrino, A. Tabano, G. Ghiringhelli, N. B. Brooker, *Europhys. Lett.* **2007**, *80*, 37003.
[25] M. Sirena, N. Haberkorn, M. Granada, L. B. Steren, J. Guimpel, *J. Appl. Phys.* **2009**, *105*, 033902.
[26] J. Rubio-Zuazo, L. Onandia, P. Ferrer, G. R. Castro, *Appl. Phys. Lett.* **2014**, *104*, 021604.
[27] K. Wang, Y. Ma, K. Betzler, *Phys. Rev. B* **2007**, *76*, 144431.
[28] S. V. Trukhanov, N. V. Kasper, I. O. Troyanchuk, M. Tovar, H. Szymczak, K. Bärner, *J. Solid State Chem.* **2002**, *169*, 85.
[29] Z. Li, M. Bosman, Z. Yang, P. Ren, L. Wang, L. Cao, X. Yu, C. Ke, M. B. H. Breese, A. Rusydi, W. Zhu, Z. Dong, Y. L. Foo, *Adv. Funct. Mater.* **2012**, *22*, 4312.
[30] K. Saito, A. Ulyanenkov, V. Grossmann, H. Ress, L. Bruegemann, H. Ohta, T. Kurosawa, S. Ueki, H. Funakubo, *Jpn. J. Appl. Phys.* **2006**, *45*, 7311.
[31] H. Z. Guo, R. Q. Zhao, K. J. Jin, L. Gu, D. D. Xiao, Z. Z. Yang, X. L. Li, L. Wang, X. He, J. X. Gu, Q. Wan, C. Wang, H. B. Lu, C. Ge, M. He, G. Z. Yang, *ACS Appl. Mater. Interfaces* **2015**, *7*, 2944.
[32] Z. Fang, I. V. Solovyev, K. Terakura, *Phys. Rev. Lett.* **2000**, *84*, 3169.
[33] M. Varela, A. R. Lupini, K. van Benthem, A. Y. Borisevich, M. F. Chisholm, N. Shibata, E. Abe, S. J. Pennycook, *Annu. Rev. Mater. Res.* **2005**, *35*, 539.
[34] C. L. Jia, M. Lentzen, K. Urban, *Science* **2003**, *299*, 870.
[35] O. L. Krivanek, M. F. Chisholm, V. Nicolosi, T. J. Pennycook, G. J. Corbin, N. Dellby, M. F. Murfitt, Ch. S. Own, Z. S. Szilagyi, M. P. Oxley, S. T. Pantelides, S. J. Pennycook, *Nature* **2010**, *464*, 571.
[36] L. Yao, S. Majumdar, L. Äkäslompolo, S. Inkinen, Q. H. Qin, S. van Dijken, *Adv. Mater.* **2014**, *26*, 2789.
[37] V. R. Galakhov, M. Demeter, S. Bartkowski, M. Neumann, N. A. Ovechkina, E. Z. Kurmaev, N. I. Lobachevskaya, Ya. M. Mukovskii, J. Mitchell, D. L. Ederer, *Phys. Rev. B* **2002**, *65*, 113102.
[38] E. Beyreuther, S. Grafström, L. M. Eng, C. Thiele, K. Dörr, *Phys. Rev. B* **2006**, *73*, 155425.
[39] M. Abbate, F. M. F. de Groot, J. C. Fuggle, A. Fujimori, O. Strebel, F. Lopez, M. Domke, G. Kaindl, G. A. Sawatzky, M. Takano, Y. Takeda, E. Eisaki, S. Uchida, *Phys. Rev. B* **1992**, *46*, 4511.
[40] J.-S. Lee, D. A. Arena, P. Yu, C. S. Nelson, R. Fan, C. J. Kinane, S. Langridge, M. D. Rossell, R. Ramesh, C. -C. Kao, *Phys. Rev. Lett.* **2010**, *105*, 257204.
[41] T. Saitoh, A. E. Bocquet, T. Mizokawa, H. Namatame, A. Fvjimori, M. Abbate, Y. Takeda, M. Takano, *Phys. Rev. B* **1995**, *51*, 13942.
[42] J.-H. Park, C. T. Chen, S-W. Cheong, W. Bao, G. Meigs, V. Chakarian, Y. U. Idzerda, *Phys. Rev. Lett.* **1996**, *76*, 4215.
[43] J. -H. Park, T. Kimura, Y. Tokura, *Phys. Rev. B* **1998**, *58*, R13330.
[44] L. Abad, V. Laukhin, S. Valencia, A. Gaup, W. Gudat, L. Balcells, B. Martínez, *Adv. Funct. Mater.* **2007**, *17*, 3918.
[45] M. Weinelt, A. Nilsson, M. Magnuson, T. Wiell, N. Wassdahl, O. Karis, A. Föhlisch, N. Mårtensson, *Phys. Rev. Lett.* **1997**, *78*, 967.
[46] K. Horiba, A. Chikamatsu, H. Kumigashira, M. Oshima, N. Nakagawa, M. Lippmaa, K. Ono, M. Kawasaki, H. Koinuma, *Phys. Rev. B* **2005**, *71*, 155420.
[47] H. Kumigashira, R. Hashimoto, A. Chikamatsu, M. Oshima, T. Ohnishi, M. Lippmaa, H. Wadati, A. Fujimori, K. Ono, M. Kawasaki, H. Koinuma, *J. Appl. Phys.* **2006**, *99*, 08S903.
[48] A. Urushibara, Y. Moritomo, T. Arima, A. Asamitsu, G. Kido, Y. Tokura, *Phys. Rev. B* **1995**, *51*, 14103.
[49] J. M. D. Coey, M. Viret, L. Ranno, *Phys. Rev. Lett.* **1995**, *75*, 3910.
[50] R. Bertacco, M. Riva, M. Cantoni, L. Signorini, F. Ciccacci, *Appl. Phys. Lett.* **2003**, *86*, 252502.
[51] J. Kanamori, *Prog. Theor. Phys.* **1957**, *17*, 177.
[52] J. B. Goodenough, *J. Phys. Chem. Solids* **1958**, *6*, 287.
[53] A. Moreo, M. Mayr, A. Feiguin, S. Yunoki, E. Dagotto, *Phys. Rev. Lett.* **2000**, *84*, 5568.
[54] J. P. Perdew, A. Ruzsinszky, G. I. Csonka, O. A. Vydrov, G. E. Scuseria, L. A. Constantin, X. Zhou, K. Burke, *Phys. Rev. Lett.* **2008**, *100*, 136406.
[55] G. Kresse, J. Furthmuller, *Phys. Rev. B* **1996**, *54*, 11169.
[56] G. Kresse, D. Joubert, *Phys. Rev. B* **1999**, *59*, 1758.
[57] A. Liechtenstein, V. Anisimov, J. Zaanen, *Phys. Rev. B* **1995**, *52*, R5467.